◆ Human Brain Mapping 37:3530–3543 (2016) ◆

Automated Alignment of Perioperative MRI Scans: A Technical Note and Application in Pediatric Epilepsy Surgery

Richard Beare,[†,*,1,7] Joseph Yuan-Mou Yang,[†,1,2,3,6] Wirginia J. Maixner,[2] A. Simon Harvey,[3,4] Michael J. Kean,[1] Vicki A. Anderson,[3,5,8,9] and Marc L. Seal[1,3]

[1]*Developmental Imaging, Clinical Sciences, Murdoch Childrens Research Institute, Melbourne, Victoria, Australia*
[2]*Department of Neurosurgery, Royal Children's Hospital, Melbourne, Victoria, Australia*
[3]*Department of Paediatrics, University of Melbourne, Melbourne, Victoria, Australia*
[4]*Department of Neurology, Royal Children's Hospital, Melbourne, Victoria, Australia*
[5]*Child Neuropsychology, Clinical Sciences, Murdoch Childrens Research Institute, Melbourne, Victoria, Australia*
[6]*Neuroscience Research, Clinical Sciences, Murdoch Childrens Research Institute, Melbourne, Victoria, Australia*
[7]*Stroke and Aging Research Group, Monash University, Melbourne, Victoria, Australia*
[8]*Department of Psychology, Royal Children's Hospital, Melbourne, Victoria, Australia*
[9]*School of Psychological Sciences, University of Melbourne, Melbourne, Victoria, Australia*

Abstract: Conventional image registration utilizing brain voxel information may be erroneous in a neurosurgical setting due to pathology and surgery-related anatomical distortions. We report a novel application of an automated image registration procedure based on skull segmentation for magnetic resonance imaging (MRI) scans acquired before, during and after surgery (i.e., perioperative). The procedure was implemented to assist analysis of intraoperative brain shift in 11 pediatric epilepsy surgery cases, each of whom had up to five consecutive perioperative MRI scans. The procedure consisted of the following steps: (1) Skull segmentation using tissue classification tools. (2) Estimation of rigid body transformation between image pairs using registration driven by the skull segmentation. (3) Composition of transformations to provide transformations between each scan and a common space. The procedure was validated using locations of three types of reference structural landmarks: the skull pin sites,

Additional Supporting Information may be found in the online version of this article.

Contract grant sponsor: Australia's National Health and Medical Research Council (Postgraduate Scholarship); Contract grant number: 1039160 (J.Y.M.Y.) and The Royal Children's Hospital Foundation; Contract grant number: RCH1000 (J.Y.M.Y.)

*Correspondence to: Richard Beare, Developmental Imaging Group, Murdoch Childrens Research Institute, Royal Children's Hospital, Flemington Rd, Parkville, Victoria, Australia 3052. E-mail: richard.beare@mcri.edu.au
[†]R.B. and J.Y.-M.Y. are the joint first authors.

Author contributions: Conception and design: Beare, Yang. Acquisition of data: Yang. Analysis and interpretation of data: Beare, Yang. Drafting the article: Beare, Yang. Critically revising the article: Anderson, Harvey, Kean, Maixner, Seal. Finally approval of the version to be published: all authors. Study supervision: Anderson, Maixner, Seal.

Received for publication 23 December 2015; Revised 3 April 2016; Accepted 29 April 2016.

DOI: 10.1002/hbm.23257
Published online 16 May 2016 in Wiley Online Library (wileyonlinelibrary.com).

the eye positions, and the scalp skin surface, detected using the peak intensity gradient. The mean target registration error (TRE) scores by skull pin sites and scalp skin rendering were around 1 mm and <1 mm, respectively. Validation by eye position demonstrated >1 mm TRE scores, suggesting it is not a reliable reference landmark in surgical scenarios. Comparable registration accuracy was achieved between opened and closed skull scan pairs and closed and closed skull scan pairs. Our procedure offers a reliable registration framework for processing intrasubject time series perioperative MRI data, with potential of improving intraoperative MRI-based image guidance in neurosurgical practice. *Hum Brain Mapp 37:3530–3543, 2016*.

Key words: accuracy; automated registration; brain shift; children; epilepsy; intraoperative; preoperative; postoperative; magnetic resonance imaging; neurosurgery; skull segmentation

INTRODUCTION

Use of preoperative magnetic resonance imaging (MRI) during neurosurgery to guide lesion resection is well established. During surgery, the skull is held fixed using a surgical frame, and surgical navigation is calibrated relative to scalp mounted fiducial markers. The main drawback is the inability to account for the effects of brain shift throughout the course of surgery. Brain shift can occur following several dynamic and interacting surgical events, such as opening the skull and the dura mater (DM), draining the cerebral spinal fluid (CSF), removing the lesion, and use of anesthetic and cerebral relaxation agents [Dorward et al., 1998; Nabavi et al., 2001; Nimsky et al., 2000, 2001; Romano et al., 2011]. The magnitude of brain shift can vary up to several centimeters, adversely impacting on the imaging-guided navigation accuracy [Hastreiter et al., 2004; Nabavi et al., 2001].

Accuracy of surgical navigation may be improved with detailed characterization of intraoperative brain shifts. Recent developments in MRI have produced intraoperative MRI scanners with similar performance to those used diagnostically [Hall and Truwit, 2008; Lipson et al., 2001]. This means that high-resolution, three-dimensional imaging data can be captured during surgery with quality comparable to that of the pre and the postoperative data, potentially allowing for correction of intraoperative brain shifts.

Aligning brain images so that common regions overlap is known as registration. It is a preprocessing step for many types of analysis and is useful for visual comparison between different MRI datasets. Intrasubject registration is commonly used to align images of the same patient acquired by different modalities or with different imaging contrasts [Fitzpatrick et al., 1998; Studholme et al., 1996, 1997; Wells et al., 1996; West et al., 1997]. Intrasubject registration may also be used to align images of the same patient acquired longitudinally, across several scanning sessions [Hajnal et al., 1995; Smith et al., 2002; Woods et al., 1998]. Characterization of intraoperative brain shift requires alignment of intrasubject, perioperative time series MRI scans. Existing studies concerning the alignment of perioperative brain MRI scans used either an interactive manual or a semi-automated registration technique.

The manual approach estimates a rigid-body transformation between the preoperative and intraoperative images using anatomical landmarks (e.g. bridge of the nose) or aligning adhesive fiducial markers placed on the scalp [Dorward et al., 1998; Nimsky et al., 2000, 2001]. The process is performed interactively between the operator guiding the registration points, and the registration software displaying the aligned images in three orthogonal planes. Registration fidelity is evaluated either visually by the operator or defined by the displacement of designated landmark/fiducial between the images. The advantage of these approaches includes the ability to update registration accuracy in real-time, and the robustness to surgical changes by ignoring landmarks affected by surgery. The disadvantages are related to interoperator variability and the time involved in manual registration. Selecting sufficient MRI visible landmarks is also difficult and labor intensive. Adhesive fiducial markers may often be removed following the initial image registration, or may shift position during the course of the surgery.

Semi-automated approaches use an automated refinement of an initial manual landmark registration [Maesawa et al., 2010; Maurer et al., 1998; Nabavi et al., 2001; Nimsky et al., 2005, 2007, 2006; Romano et al., 2011]. Automated methods, widely used in brain imaging studies, estimate a transformation between images by maximizing a voxel similarity measure (or minimizing a voxel dissimilarity measure) [Woods et al., 1992, 1993]. Typically, the similarity measure is computed using all or most of the image. Automated approaches are widely available and can estimate rigid-body transformations quickly. They have been shown to be more accurate than manual landmark approaches [Alpert et al., 1996; Sarkar et al., 2005; Strother et al., 1994; Zuk and Atkins, 1996]. Subvoxel registration accuracy has been demonstrated with automated approaches in well-constrained scenarios using simulated phantom images [Hajnal et al., 1995; Woods et al., 1998], normal intrasubject MRI data [Hajnal et al., 1995; Strother et al., 1994; Woods et al., 1998] and cross-modality data (i.e., PET-MRI, CT-MRI) [Alpert et al., 1996; Fitzpatrick

et al., 1998; Sarkar et al., 2005; Strother et al., 1994; Studholme et al., 1997; West et al., 1997; Zuk and Atkins, 1996].

Automated approaches are extremely effective at aligning images with differing geometry and contrast, but inaccuracies can occur when content differs, for example when aligning brains before and after resection. This occurs because the resected region contributes to the similarity measure. It is possible to use masking strategies to constrain the similarity function calculation to common areas, but this is both manually demanding and can cause optimization problems [Jenkinson and Smith, 2001]. Similar problems occur with non-brain tissue in neuroimaging studies, where face and scalp differ significantly between individuals and reduce brain registration accuracy. Widely used neuroimaging tools, such as Statistical Parametric Mapping (SPM) and the FMRIB Software Library (FSL) address the issue in different ways. SPM combines tissue classification and registration so that the contribution of non-brain tissues can be down weighted while FSL performs a brain extraction step prior to registration.

The automated registration approaches driven by the brain voxels inherently bias brain shift characterization by removing or minimizing components of brain tissue changes relative to the skull, as well as being biased by changes caused by the surgery. In an extreme example, a "perfect" brain registration would eliminate all differences in brain tissue morphology.

In this technical note, we introduce and validate an automated registration procedure that is driven by the skull anatomy instead of depending on brain tissue matching. The skull is a logical choice of anatomical structure to use for registration because it is held fixed in the surgical scenario. We also validate the registration between the preoperative and the postoperative MRI scans so the technique can be applied to other quantitative MRI research, such as exploring adaptive brain changes and recovery following operations. The alignment method is automated, thus avoiding the operator-dependent bias associated with manual landmark selection or mask creation. The procedures are implemented using widely available computational neuroimaging software. We demonstrate the feasibility, reliability, and clinical utility of this registration procedure using the perioperative MRI scans acquired clinically in 11 pediatric epilepsy surgery patients.

THEORY

The alignment procedures described in this note use two computational tools—brain tissue classification and registration, both of which are widely used in neuroimaging research. Both brain tissue classification and registration have been the subject of significant research effort in the past 20 years (See [Isgum et al., 2015; Mendrik et al., 2015; Murphy et al., 2011] for recent reviews of public challenges) and many implementations of them are openly available in the neuroimaging community [Ashburner and Friston, 2005; Avants et al., 2011; Jenkinson and Smith, 2001; Klein et al., 2010; Smith et al., 2004].

Registration accuracy is typically estimated by computing distances between corresponding landmarks in images after alignment to produce a target registration error (TRE). Perfect registration will produce a zero TRE. Common examples of landmarks include easily identifiable anatomical features such as the bridge of the nose or adhesive fiducial markers. It is important to note that localizing the position of landmarks introduces error which will be included in the TRE—thus accuracy estimates based on landmarks are likely to be conservative as they include errors in landmark position that are not related to registration.

The validation procedure uses several image processing tools (to accurately segment landmarks) from the field of mathematical morphology. They are morphological filtering and morphological segmentation using the watershed transform from markers (WTM). Theoretical aspects of these tools are discussed in the Supporting Information.

MATERIALS AND METHODS

MRI Alignment Procedure and Accuracy Validation

Skull segmentation

The "New Segment" procedure, implemented in the SPM software version 8, was used for brain tissue, skull, and scalp segmentation (Fig. 1). "New Segment" is a development of the Unified Segmentation algorithm that combines tissue classification, bias inhomogeneity correction and alignment to an atlas [Ashburner and Friston, 2005].

Intrasession sequence image alignment

Intrasession sequence alignment may be performed to estimate transformations between the T1-weighted image and other images acquired in the same session, thus allowing other types of information to be transformed to the common space. An overview of approaches and applications is provided in discussion. The transformation between sequences may be linear when distortion is minimal or non-linear when distortion is significant, as can occur with echo-planar imaging (EPI) sequences. Both linear and non-linear distortions can be composed to produce transformations to standard space, as indicated in Figure 2.

Pairwise inter time point image alignment

Transformations between pairs of T1-weighted scans were estimated using the FLIRT-based procedure introduced in the SIENA tool, but using the SPM derived skull segmentation in place of the original skull boundary used in SIENA. Transformations to the halfway space between scan pairs were also computed using the SIENA tool.

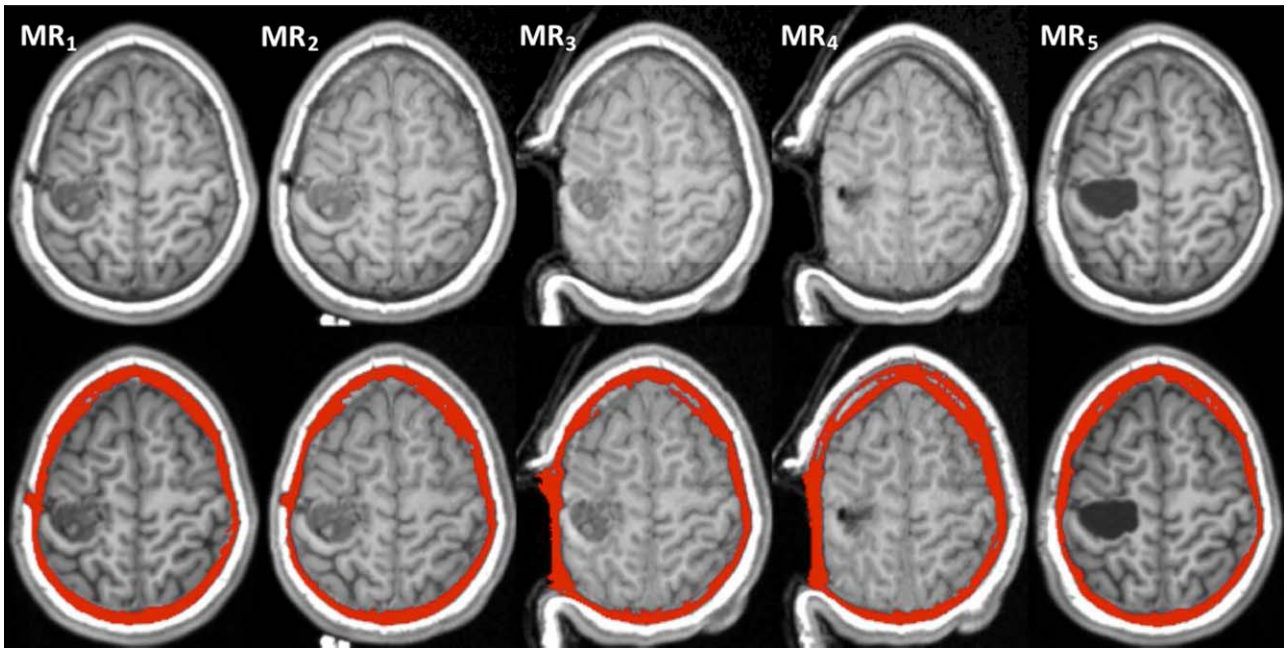

Figure 1.
A case example (Patient 4) of axial T1-weighted MRI (top row) with overlaid SPM derived skull segmentation (bottom row, in red) over five consecutive perioperative time points (MR_1 to MR_5). Skull is opened in time points MR_3 and MR_4 and the skull classification procedure interpolates the missing regions. [Color figure can be viewed in the online issue, which is available at wileyonlinelibrary.com.]

Composition of all pairwise transformations into a single transformation

The pairwise transformations between pairs of T1-weighted scans acquired at different times and between the T1-weighted scan and the diffusion-weighted imaging (DWI) sequences acquired in the same session were then composed to map all images to a common space. We used the halfway space between images from the first two sessions as the common space. The procedure is illustrated in Figure 2.

Registration accuracy measures

The accuracy of registration was evaluated using two types of landmark and a surface comparison method. One set of landmarks (skull pin sites) was only visible during surgical scans while the second set of landmarks (eye globe positions) and scalp surface comparison approaches were applicable to all scans. Landmarks were selected to be independent of the information used in registration, easily identifiable on T1-weighted images and fixed during surgery. Semi-automated approaches were used to determine landmark locations in order to reduce bias.

TRE was computed for the two landmark approaches. The median of displacements between corresponding points on a pair of scalp surfaces provided the equivalent comparison for surfaces. Median values were used to reduce the impact of outliers.

The following describes the segmentation methods for each landmark/structure used to evaluate the registration accuracy.

Fixed skull landmark: skull pin sites. During surgery, the skull position was held constant using a surgical head frame with three skull pins. The metallic pins produced susceptibility artifacts that were clearly visible on T1-weighted images (Fig. 3A). The pin sites were segmented using a semi-automated approach and the centroid of the segmentation used as the landmark location.

Pin sites were segmented as follows:

1. An approximate manual segmentation of each pin site was created in the first intrasurgical scan. This segmentation included all of the pin site and a moderate amount of surrounding tissue and empty space (Fig. 3B) and was used to indicate the pin location. This segmentation was refined by the subsequent steps.
2. A segmentation of the entire head was created from the presurgical scan using Otsu thresholding [Otsu, 1975], followed by a morphological closing (15 mm spherical structuring element) and a morphological opening (10 mm spherical structuring element), retaining the

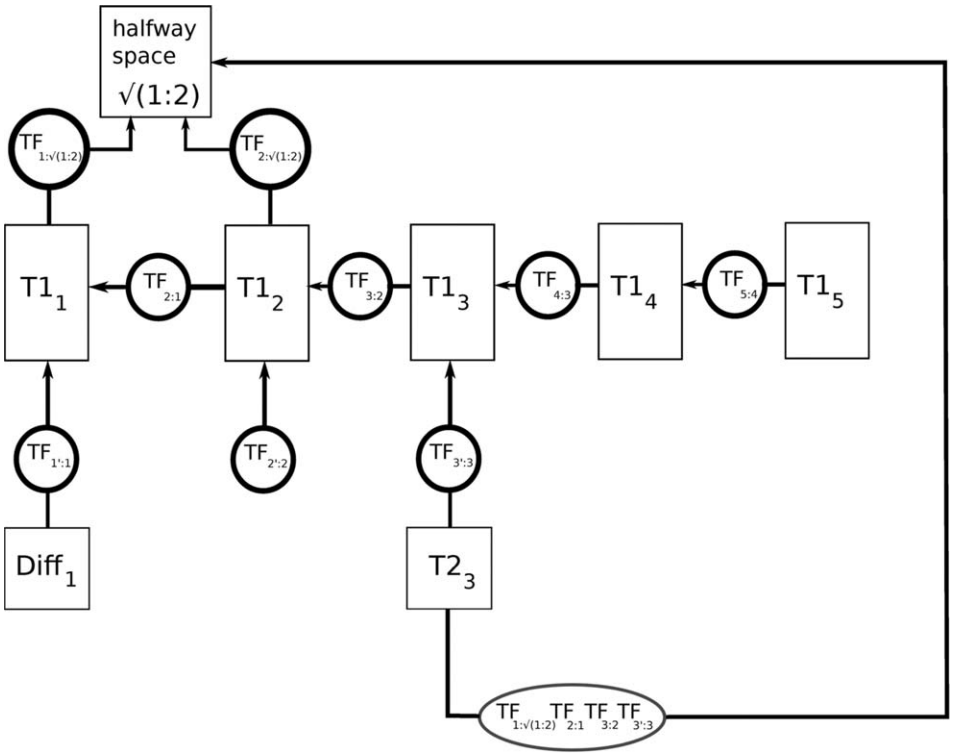

Figure 2.

Alignment of images to a common space via composition of pairwise transformations. $T1_1$ through $T1_5$ are T1-weighted scans at five perioperative time points. $Diff_1$ is a presurgical DWI scan, and $T2_3$ is a T2-weighted intrasurgical MR scan acquired in the corresponding MR sessions. Circles and ellipses indicate transformation between images. Transformations (TF) between the T1-weighted and the other scans acquired in one session are estimated first. This is annotated using $TF_{x':x}$, where "x" represents the acquisition time point. For example, $TF_{1':1}$ represents transformation of $Diff_1$ to $T1_1$. Next, transformations are estimated between pairs of T1-weighted scans ($TF_{(x+1):x}$). For example, transformation $TF_{2:1}$ aligns $T1_2$ with $T1_1$. Transformation to the halfway space between pairs (e.g. $TF_{1:\sqrt{1:2}}$) can be computed from the between-pair transformations. Pairwise transformations are then combined to produce a transformation between any image and the halfway space between the first two scans. For example, the transformation $TF_{1:\sqrt{1:2}}TF_{2:1}TF_{3:2}TF_{3':3}$ aligns the T2 scan from MR session three with the common space.

largest connected component and then applying a 5 mm morphological dilation. This segmentation was used to mask aspects of surgical scans, such as the craniotomy site.

3. Automated morphological filtering methods were used to refine this manual segmentation:
   a. The intrasurgical T1-weighted scan was masked using the head segmentation produced in Step 2.

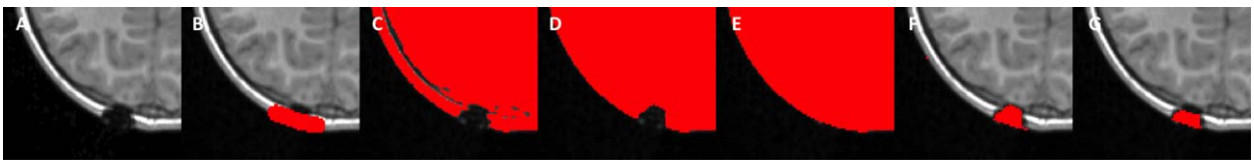

Figure 3.

Skull pin site segmentation steps. (**A**) T1-weighted image showing the artifact of the metallic skull pin, (**B**) manual approximate segmentation, (**C**) thresholding of brain to produce mask, (**D**) small morphological closing to remove small gaps in mask, (**E**) large closing to remove large holes in mask, (**F**) difference between E and D recovers the large holes in the mask, (**G**) masking with B and retaining largest three components to produce the final pin site segmentations. [Color figure can be viewed in the online issue, which is available at wileyonlinelibrary.com.]

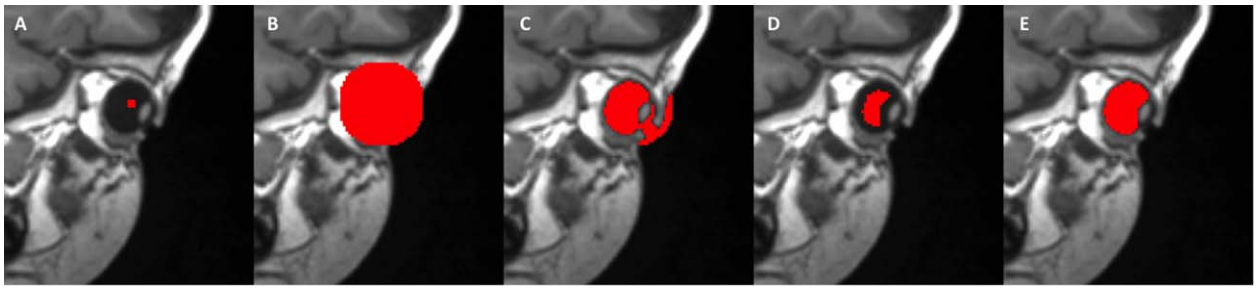

Figure 4.

Eye globe segmentation steps. (**A**) Manually mark approximate center of the eye globe, (**B**) dilation of center to create a region of interest including the entire eye globe, (**C**) thresholding of eye region (retaining dark voxels) to produce mask of interior of eye globe, (**D**) erosion and retain component connected to original point in A, to disconnect interior of eye from surrounding dark voxels, (**E**) dilation to reverse the effect of the erosion and produce the final eye globe segmentation. [Color figure can be viewed in the online issue, which is available at wileyonlinelibrary.com.]

b. The masked T1-weighted scan was thresholded using Otsu's method (Fig. 3C).
c. A morphological closing (radius 3 mm) applied to fill small dark regions such as the skull and CSF (Fig. 3D).
d. A large morphological closing (radius 30 mm) applied to fill pin sites (and other larger dark regions such as ventricles, eyes etc) (Fig. 3E).
e. The differences between images from Steps c and d (Fig. 3F) was masked using the rough manual segmentation and the largest three connected components retained to produce segmentation of the pin sites (Fig. 3G).

Eye globe positions landmark

The eye globes within the orbital fossa were segmented using a semi-automated approach and the center of gravity of the segmentation used as the landmark location. It was used to assess registration accuracy of all pairings of perioperative MRI.

Eye globes were segmented using the following semi-automated approach:

1. The approximate center of each eye globe was marked in the presurgical scan (Fig. 4A).
2. A morphological dilation (15 mm) was applied to the eyeball marker to create a region of interest containing the entire eye globe (Fig. 4B).
3. The region of interest from Step 2 in T1-weighted scan was threshold using the triangle method [Zack et al., 1977] to produce mask of interior of the eye globe (Fig. 4C).
4. A morphological erosion (3 mm) was applied to the image from Step 3 to retain the components connected to the original marker (Fig. 4D) and a morphological dilation (3 mm) was applied (Fig. 4E) to reverse the effect of the erosion and produce the final eye globe segmentation.

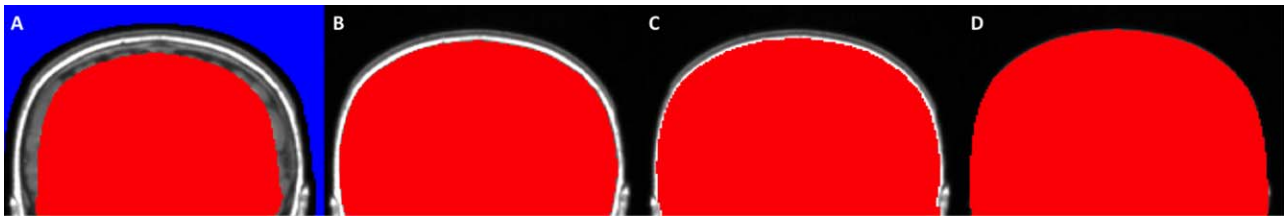

Figure 5.

Scalp skin surface segmentation steps using the WTM. (**A**) stage I markers derived from head segmentation, with background marker in blue and foreground marker in red, (**B**) inner edge of scalp adipose connective tissue layer obtained by applying a WTM to detect the peak increasing gradient, (**C**) peak of the scalp adipose connective tissue layer detected using stage B result as the foreground marker and applying WTM to the intensity image, (**D**) skin surface detected using a WTM with a dilated stage C result as the foreground marker and detecting peak decreasing gradient. [Color figure can be viewed in the online issue, which is available at wileyonlinelibrary.com.]

TABLE I. Participant information: basic demographics, epilepsy pathology, and epilepsy surgery

Patient ID	Age (years)	Gender	Epilepsy lesion pathology	Lesion hemisphere	Lesion site	Resected lesion volume (cm^3)	Surgical head position	Craniotomy area (cm^2)
1	13.4	Female	Cerebral gliosis secondary to previous resection of pilocytic astrocytoma	L	F	3.9	Supine lateral	81.0
2	13.4	Male	FCD	L	T	16.5	Lateral	55.3
3	3.8	Male	TSC	R	F, T[a]	9.5[a]	Supine lateral	48.8
4	15.8	Male	DNET	R	F	13.5	Lateral	32.4
5	15.5	Male	Chronic encephalitis	L	F	12.4	Lateral	82.5
6	4.8	Male	FCD with DVA	L	F	3.9	Lateral	37.5
7	10.2	Female	Non-specific pathology	R	T	31.5	Lateral	20.0
8	10.9	Female	DNET	R	O	7.0	Oblique lateral	22.0
9	13.3	Female	DNET	L	T/P/O junction[b]	5.2	Lateral	19.6
10	15.4	Female	TSC	R	O	4.6	Oblique lateral	20.3
11	12.2	Female	DNET	R	T/P/O junction[b]	24.2	Oblique lateral	35.8

[a]Multiple cortical lesions were resected in these cases. Combined volumes of these lesions were represented here.
[b]T/P/O junction included lesions involving either the subcortical WM or cortical regions of the supramarginal gyrus, angular gyrus, posterior portions of the middle and inferior temporal gyri, or the fusiform gyrus.
Abbreviations: BOSD: bottom of sulcus dysplasia; cc: cubic centimetre; cm: centimetre; DNET: dysembryoplastic neuroepithelial tumour; DVA: developmental venous anomaly; F: frontal; FCD: focal cortical dysplasia; I: insula; L: left; O: occipital; P: parietal; R: right; T: temporal; TSC: tuberous sclerosis complex.

Scalp skin surface layer

The surface of the scalp skin was clearly visible on T1-weighted MRI scans. A useful proportion was relatively stable during surgery (see discussion for exceptions) and the extracted surface was therefore useful for assessing registration accuracy. Regions of the skin surface remote from pin sites, eyeballs, and surgical resection were used to assess registration accuracy. The face and neck soft tissues were cropped out, below a plane between the eyes and the basion of the foramen magnum.

The surface was segmented using several phases of WTM applied to the T1-weighted scan and gradients. The multiphase approach was found to be more reliable than a single phase as the magnitude of the gradient between air and skin was often similar to the gradient between skin and adipose tissue (within the scalp connective tissue layer). Adipose tissue appears brightest in the scalp on T1-weighted scans.

1. Markers were derived from a presurgical head mask (as described in the pin site segmentation) (Fig. 5A).
2. The inner edge of the scalp adipose tissue layer was segmented by applying a WTM to a gradient image containing dark to light transitions (Fig. 5B).
3. The peak intensity of the scalp adipose tissue layer was segmented (Fig. 5C) using a WTM with the T1-weighted intensity as the control image and markers derived from the Step 2 result.
4. The skin surface was segmented (Fig. 5D) by applying a WTM to a gradient image containing light to dark transitions and markers derived from the Step 3 result.

Analysis

TRE was computed for pairs of MRI scans. The notation $MR_{1:2}$ denotes the TRE measure between MRI scans at time points 1 and 2.

Both means and medians were calculated to represent the center of the TRE distribution. The range, interquartile range (IQR), standard deviation (SD), and 95% confidence interval (CI) were calculated to represent the dispersion of the TRE distribution.

Patients and MRI Acquisitions

Participants

We prospectively recruited 11 children undergoing surgery for drug-resistant focal epilepsy, presenting to the Royal Children's Hospital, Melbourne, Australia (five males and six females; average age 11.7 years, range 3.8 to 15.8 years). Basic demographics, and information pertaining to their epilepsy pathology and surgery are summarized in Table I.

The study complied with the Australia's National Health and Medical Research Council (NHMRC) National Statement on Ethical Conduct in Human Research (2007) and the Note for Guidance on Good Clinical Practice (CPMP/ICH-135/95). The Hospital's Research Ethics Committee approved the study. All parents and guardians, and cognitively competent participants older than 12-year-old gave informed consent prior to study commencement.

TABLE II. Summary of TRE for all scan pairs using the three different registration validation landmarks

Validation Landmarks	TRE (mm)					
	Mean	SD	95%CI	Median	IQR	Range
Skull pins	0.95	0.93	0.69–1.21	0.80	0.53–1.04	0.13–6.03
Eye globes	2.11	1.15	1.85–2.37	1.92	1.35–2.60	0.22–6.42
Skin surface	0.59	0.26	0.50–0.67	0.54	0.38–0.74	0.20–1.22

Abbreviations: CI: confidence interval; IQR: interquartile range; SD: standard deviation.

IMAGE ACQUISITION

Up to five consecutive perioperative MRI scans were acquired for the study participants.

MR_1: Presurgical image used for surgical planning, acquired within several months before the surgery (average 3.7 months; range 4 days–6.8 months prior to surgery).

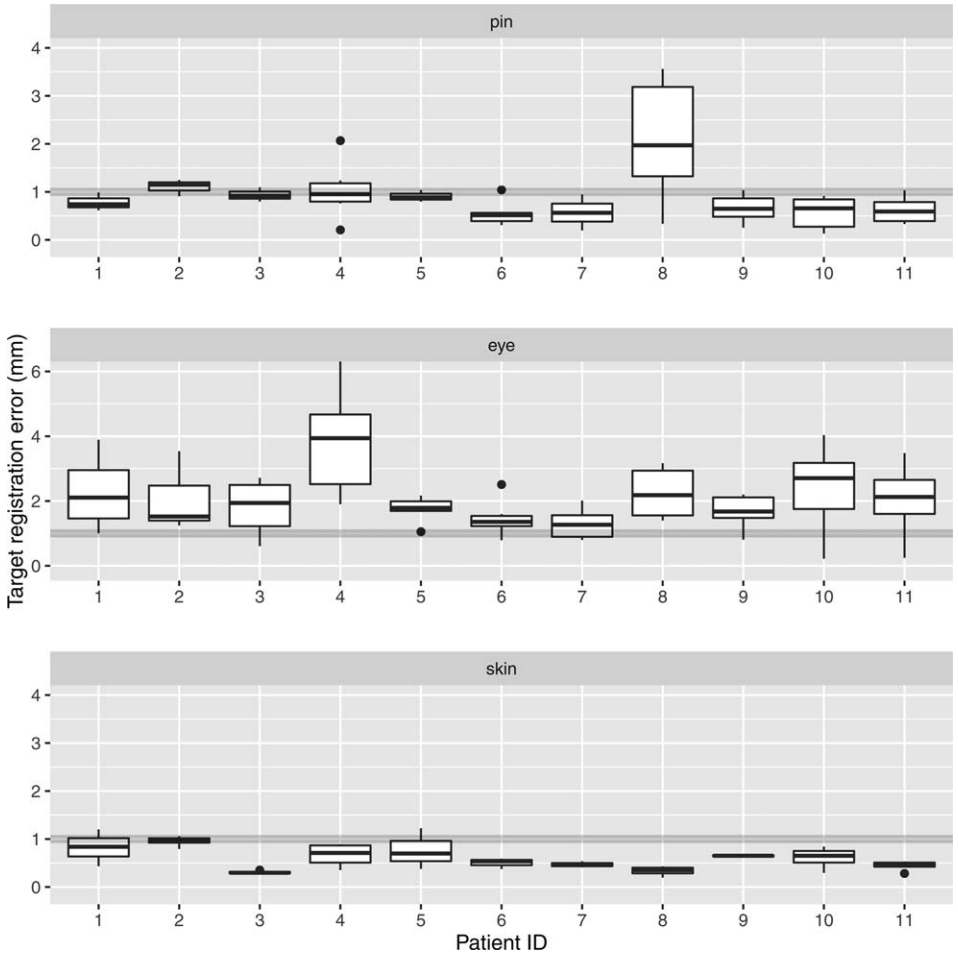

Figure 6.

The box and whisker plots showing the TRE for all patients estimated using the skull pin sites, the eye globe positions and the scalp skin surface comparisons. The 1 mm TRE lines are marked on all plots to aid interpretation. All TRE scores estimated using the scalp skin surface comparisons are below 1 mm. All except two patients' TRE scores estimated using the skull pin sites are at or below 1 mm. In Patients 4 and 8, erroneous outlier maximum TRE scores contribute to the unusually high TRE scores. Majority of the TRE scores estimated using the eye globe positions are above 1 mm.

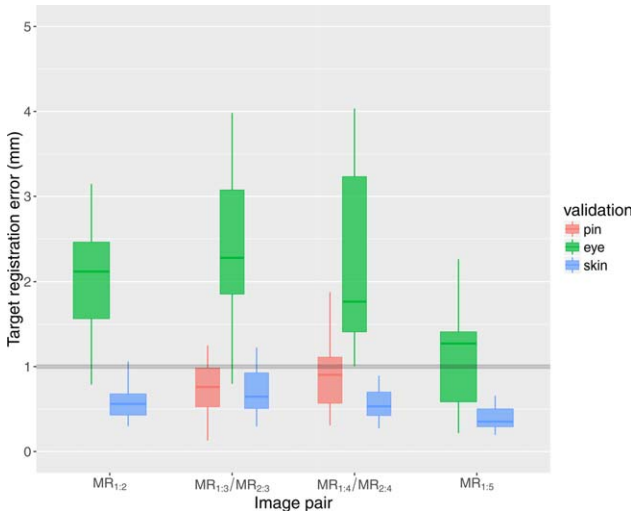

Figure 7.

The box and whisker plot of TRE scores by MRI pairs using the skull pin site, and the eye globe position validation landmarks and the scalp skin surface comparisons. The 1 mm TRE line is marked on the plot to aid interpretation. The TRE scores based on skull pin sites are only available for the intraoperative scan pairs ($MR_{2:3}$ and $MR_{2:4}$). For the validation method using the scalp skin surfaces, the estimated TRE scores between opened and closed skull scans ($MR_{1:3}$ and $MR_{1:4}$) are not significantly different from those achieved between closed skull scans ($MR_{1:2}$ and $MR_{1:5}$) ($P = 0.12$, mixed effects model). [Color figure can be viewed in the online issue, which is available at wileyonlinelibrary.com.]

MR_2: First intrasurgical image acquired with the patient's head fixed in the surgical position prior to craniotomy.

MR_3: Second intrasurgical image acquired post skull opening (craniotomy), and DM opening (durotomy), prior to lesion resection.

MR_4: Third intrasurgical scan acquired post lesion resection, prior to closure of the skull.

MR_5: Follow-up scan acquired approximately three months postsurgery (average 3.3 months; range 2.6 months to 4.3 months following surgery).

Presurgical and postsurgical scans were obtained using a 32-channel head coil 3Tesla (3T) Siemens MRI scanner (Siemens Magnetom Trio Tim syngo MRI, Erlangen, Germany). Intrasurgical scans were obtained using an 8-channel head coil 3T movable intraoperative Siemens MRI scanner (IMRIS, Manitoba, Canada) placed in an operating theatre with radiofrequency shielding.

The acquisition sequences were identical in all cases. Non-contrast T1-weighted high-resolution magnetization prepared rapid gradient-echo data were the selected anatomical sequence used for registration purposes (For the presurgical and the postsurgical scans: 256 × 256 acquisition matrix, FOV = 250, 0.8 mm^3 isotropic voxels, TR/TE = 1,900/2.69 ms; For the intrasurgical scans: 256 × 256 acquisition matrix, FOV = 256, 1.0 mm^3 isotropic voxels, TR/TE = 1,800/2.19 ms).

RESULTS

The patients and their operations were typical of those managed in a tertiary pediatric epilepsy surgical center (Table I).

Overall, 54 out of a possible 55 MRI scans were acquired from all patients. MR_1, MR_2, MR_3, and MR_5 scans were acquired from all patients and used for analysis. Two of the MR_1 and the MR_5 scans were acquired under general anesthesia. MR_4 scans were acquired in 10/11 patients. One MR_4 scan was not performed due to safety and logistic issues related to the long surgical time. Two MR_4 scans were excluded from analysis. One had poor image quality, as a result of significant EPI susceptibility distortion and head motion artifact. The other had incomplete acquisition due to MRI hardware malfunction.

The TRE scores are summarized in Table II. Both the mean and median TRE scores were larger with the eye globe measures than those obtained from using the skull pins and scalp skin surface measures. The mean and median TRE scores of the latter two measures were below 1 mm, approximately equate to the MRI voxel dimension. The ranges of TRE scores for both the eye globe and skull pin measures were greater than those from the scalp skin surface measure, due to outlier effects (see discussion).

The TRE scores by each patient are shown in Figure 6. The TRE scores obtained with eye globe measures were above 1 mm for 14/15 patients. The TRE scores obtained

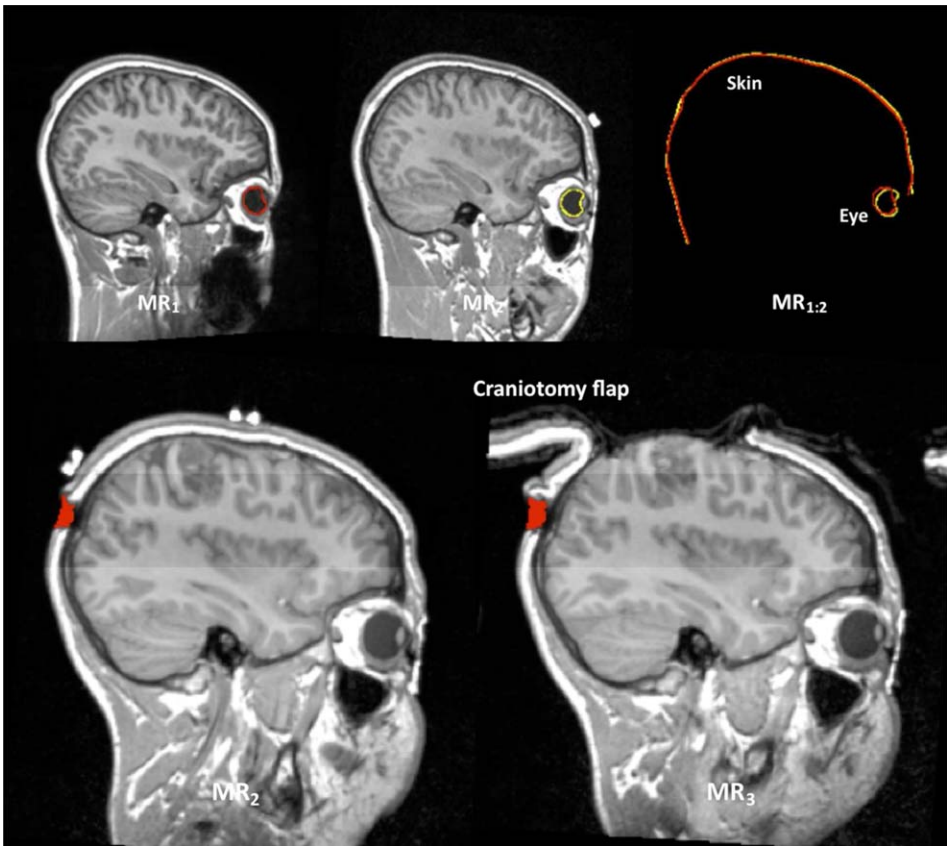

Figure 8.

Sources of TRE in Patient 4. (**A**) Notable differences in eye globe positions between pairings of preoperative (red) and first intraoperative (yellow) MRI scan, while scalp skin surfaces are closely aligned. (**B**) Rotational deformation of skin surrounding the skull pins, and skin compression close to the craniotomy flap lead to segmentation error of the skull pin site (in red). This causes an overestimation of the registration error. Abbreviations: $MR_{1:}$ the presurgical scan; $MR_{2:}$ the first intrasurgical scan; $MR_{3:}$ the second intrasurgical scan; $MR_{1:2:}$ the aligned pair of MR_1 and MR_2. [Color figure can be viewed in the online issue, which is available at wileyonlinelibrary.com.]

from scalp skin surface comparisons were all below 1 mm, and equated approximately to the MRI voxel dimensions. All except two patients' TRE scores obtained from skull pin sites were at or below 1 mm. In Patients 4 and 8, the largest TRE scores were 2 mm and 6 mm respectively, caused by surgical factors influencing segmentation of the skull pin sites (see discussion).

When summarizing the results by MRI pairs, the TRE scores estimated from the skin surface did not significantly differ between pairings of scans with closed: opened ($MR_{1:3}$ and $MR_{1:4}$) and closed: closed ($MR_{1:2}$ and $MR_{1:5}$) skull ($P = 0.12$, using mixed effects model) (Fig. 7). The mean TRE scores for scalp skin surface comparisons were 0.58 mm (SD 0.22; 95% CI 0.43–0.73) for $MR_{1:2}$, 0.71 mm (SD 0.33; 95% CI 0.49–0.93) for $MR_{1:3}$, 0.56 mm (SD 0.20; 95% CI 0.43–0.70) for $MR_{1:4}$, and 0.27 mm (SD 0.27; 95% CI 0.19–0.70) for $MR_{1:5.}$ The mean TRE scores for eye globe landmarks were 2.07 mm (SD 0.78; 95% CI 1.73–2.42) for $MR_{1:2}$, 2.52 mm (SD 1.22; 95% CI 1.98–3.06) for $MR_{1:3}$, 2.38 mm (SD 1.31; 95% CI 1.80–2.96) for $MR_{1:4}$, and 1.10 mm (SD 0.65; 95% CI 0.73–1.48) for $MR_{1:5}$.

The TRE scores based on skull pin locations were only available for the intraoperative scans. The mean TRE scores estimated from the skull pin sites were 0.82 mm (SD 0.63; 95% CI 0.60–1.04) for $MR_{2:3}$ and 1.19 mm (SD1.30; 95% CI 0.54–1.84) for $MR_{2:4}$.

DISCUSSION

Characterization of perioperative brain shifts requires accurate registration of MRI scans acquired prior to, during and after surgery. In this technical note, we introduce and validate an automated registration procedure that is driven by skull segmentation, thus avoiding biases that may be introduced if the registration is driven by the brain tissue. The automated alignment methods prevent operator-dependent

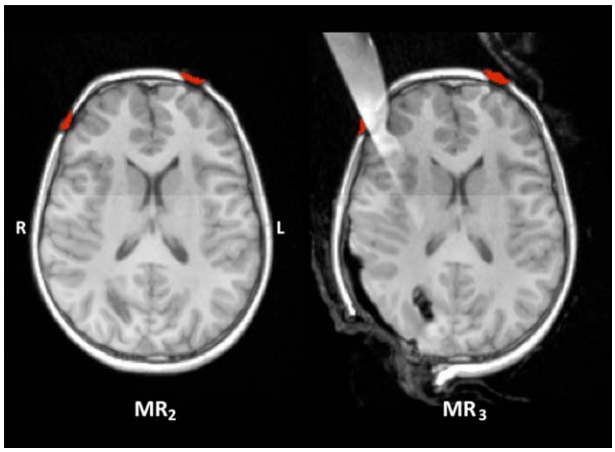

Figure 9.

Error in segmentation of the skull pin sites for Patient 8. The front right skull pin site (red) is obscured by wrap around artifact incorporating extracranial soft tissue into the field of view. This leads to segmentation error of this skull pin site, thus overestimation of the TRE. Abbreviations: L: left; MR_2: the first intrasurgical scan; MR_4: the third intrasurgical scan; R: right. [Color figure can be viewed in the online issue, which is available at wileyonlinelibrary.com.]

biases associated with manual landmark selection or mask creation. They are implemented using widely available computational neuroimaging software.

The methods described were applied to data acquired in a pediatric epilepsy surgery setting, and the adhesive fiducial markers were not available for all MRI scans. We used both landmark based and surface based approaches to evaluate registration accuracy, with one traditional structure landmark (center of eye globe) and one novel landmark (susceptibility artifacts from skull pins of the surgical head frame) as well as a precise segmentation of the scalp skin surface. The skull pin sites were only available on the intraoperative MRI scans.

Registration using our automated skull-based approach is very precise, with sub-voxel, sub-millimeter accuracy across all time points according to surface-based validation, and approximately 1 mm accuracy using pin site landmarks. The lower accuracy measured using eye globe landmarks suggests they are not reliable in the surgical scenario. While all eye globe segmentation appeared to be visually satisfactory, multi-millimeter differences in eye position were observed on different time series MRI scans of many patients. These subtle differences were possibly related to eye movements during awake scanning or relaxation of eye muscles during general anesthesia. Figure 8A demonstrates an example of this eye position segmentation error in one patient. Alternative anatomical features or skull bony landmarks were not chosen to evaluate the registration accuracy because they require manual definition, introducing apriori biases.

The study also demonstrated accurate image registration can be achieved between intraoperative pre and post skull opening MRI scans. This capability is due to the behavior of the SPM "New Segment" tissue classification in the presence of missing skull. Tissue classification algorithms, such as those derived from SPM, are designed to support

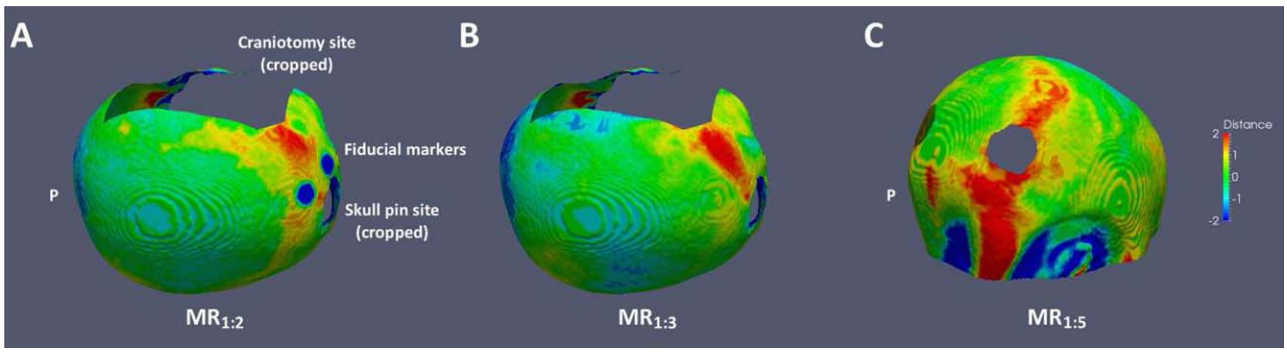

Figure 10.

Three-dimensional renderings of skin scalp surface illustrating distribution of estimated surface displacement between time points. Localized skin deformation is visible in different MRI pairings. (**A**) Alignment pairing between the presurgical and the first intrasurgical scans ($MR_{1:2}$). The image is displayed in a right lateral operative position for a left temporal craniotomy. The craniotomy and the skull pin sites are cropped out. Note greater registration errors occur over the frontal scalp region, relating to the application of adhesive skin fiducial markers (in blue), and tractional skin changes adjacent to the skull pin site. (**B**) Alignment pairing between the presurgical and the second intrasurgical scans ($MR_{1:3}$). Additional registration error is noted around edges of the craniotomy flap (in cyan). (**C**) Alignment pairing between the presurgical and the postsurgical scans ($MR_{1:5}$). Right posterior skull view is displayed. Greater registration errors are noted around the ear (likely due to skin compression associated with headphone use), and around the occiput and the neck (likely due to supine positional skin compression). Abbreviation: p: posterior. [Color figure can be viewed in the online issue, which is available at wileyonlinelibrary.com.]

studies of typical brains, or ones with relatively typical anatomical architecture and thus can perform poorly in the presence of pathology or contrast agents, with misclassification of brain tissues. However, the skull classification tends to be minimally affected by such errors. Due to the minimal contrast between skull and air in T1-weighted images, the skull classification tends to interpolate across a craniotomy defect (see Fig. 1).

While this is an incorrect classification, it is a useful method of approximation for the purpose of skull alignment. It reduces the difference between the surgical and the non-surgical skull segmentations and thus improves the registration process. The registration accuracy between the opened and the closed skull scans does not significantly differ from those achieved with aligning the closed skull scans (Fig. 7). This is an important affirmation of our registration technique, from which the degree of brain shifts can be studied over multiple perioperative time points.

The amount of clinically acceptable registration error is likely to be case and scenario dependent. Existing brain shift studies utilizing pre and intraoperative MRI data reported a root mean square displacement of TRE score around 1.0 to 1.5 mm, and a range between 0 to 3.7 mm [Nimsky et al., 2000, 2001, 2006]. In other studies, the registration accuracy was either not addressed [Maesawa et al., 2010; Ozawa et al., 2009; Romano et al., 2011] or limited only to visual inspection of image overlays [Maurer et al., 1998; Nabavi et al., 2001; Nimsky et al., 2005, 2007]. In studies with reported TRE scores, image registrations were performed using software incorporated in the surgical navigation system—one required manual fiducial matching [Nimsky et al., 2000] and the other two used semi-automated algorithm based on mutual information/voxel similarity measures [Nimsky et al., 2001, 2006]. Our reported TRE scores using the skull pins and scalp skin surface as validation measures achieve at least comparable registration accuracy with these reported values.

Our results are also comparable to those obtained from automatic registration performed in normal intrasubject time series MRI data with simulated image interpolation [Hajnal et al., 1995; Strother et al., 1994; Woods et al., 1998]. Our results also compare favorably to registration accuracy achieved using normal cross-modality data (i.e,. MRI-PET, MRI-CT, and MRI-SPECT registration) [Alpert et al., 1996; Pfluger et al., 2000; Sarkar et al., 2005; Strother et al., 1994; West et al., 1997].

The accuracy of registration is likely to be an underestimate. Susceptibility artifacts change between scans and segmentation of them is variable. Estimation of skull pin location is thus subject to error, and the error inflates the registration error. Other MRI artifacts, if extending over these pin locations, can also add to this segmentation error. This is the reason for an outlier pin site TRE score observed in one patient, as illustrated in Figure 9.

The effects of the surgical frame, craniotomy and head position on the scalp skin surface are surprisingly complex and are detectable in skin surface renderings. Compression or deformation of scalp skin by application of the surgical frame, differences in muscle state caused by head position, and extended effects of the craniotomy all change the skin surface in subtle ways (Fig. 10). These changes in surface shape contribute to measures of registration error. Figure 8B illustrates an example of this skin surface rendering problem, leading to overestimation of registration error by skull pin segmentation in one patient. We have used a robust statistic (median) to summarize the registration error derived from the surfaces, but the accuracy likely remains an underestimate.

Intrasession alignment offers the potential to align information from different scan types in a common space. For example, using phase reversed acquisitions or field mapping a distorted preoperative DWI sequence may be aligned with the T1-weighted scan from the same session, allowing tractography results to be aligned in the common space [Cusack and Papadakis, 2002; Irfanoglu et al., 2015; Jezzard and Balaban, 1995]. Alternatively, an intraoperative contrast-enhanced scan providing information about remaining lesional tissue could be transformed to the common space to allow comparison with the presurgical planning data.

Internal inconsistency associated with MRI hardware and the scanning environment inherently limits the degree of registration accuracy that can be achieved in this study. Scan-to-scan variability occurs with noises, motion artifacts (head movement, cardiac and CSF pulsation), anatomic mis-mapping associated with signal wrap around, image distortion related to magnetic field and gradient field inhomogeneity, radiofrequency noise, and signal attenuation associated with surface coil distances. Interscanner variability also exists because we processed MRI data acquired by a conventional and an intraoperative 3T MRI scanner.

Findings of this work have provided us with the technical affirmation required to implement this registration procedure to the study of intraoperative brain and white matter tract shifts. Applicability of our registration procedure requires further evaluation of its computation time and in alternative clinical scenario. Technical issues surrounding software integration within the surgical navigation systems also need to be addressed first.

ACKNOWLEDGMENTS

We gratefully thank the operating theatre nurses, anesthetic staff and MRI technologists involved in MRI data acquisition, and the families and children who participated in this study. We thank Dr. Christopher L. Adamson, PhD, for technical support. This research was conducted within the Developmental Imaging research group, Murdoch Childrens Research Institute at the Melbourne Children's MRI Centre, Royal Children's Hospital, Melbourne, Victoria. It was supported by the Royal Children's Hospital, Murdoch Childrens Research Institute, The University of Melbourne Department of Paediatrics, and the Victorian Government's Operational Infrastructure Support

Program. Disclosure: All authors report no disclosures relevant to the manuscript. W. J. Maixner receives royalties from Springer- Verlag for the books *Pediatric Hydrocephalus* and *Spinal Bifida*.

REFERENCES

Alpert NM, Berdichevsky D, Levin Z, Morris ED, Fischman AJ (1996): Improved methods for image registration. Neuroimage 3:10–18.

Ashburner J, Friston KJ (2005): Unified segmentation. Neuroimage 26:839–851.

Avants BB, Tustison NJ, Wu J, Cook PA, Gee JC (2011): An open source multivariate framework for n-tissue segmentation with evaluation on public data. Neuroinformatics 9:381–400.

Cusack R, Papadakis N (2002): New robust 3-D phase unwrapping algorithms: Application to magnetic field mapping and undistorting echoplanar images. Neuroimage 16:754–764.

Dorward NL, Alberti O, Velani B, Gerritsen FA, Harkness WF, Kitchen ND, Thomas DG (1998): Postimaging brain distortion: Magnitude, correlates, and impact on neuronavigation. J Neurosurg 88:656–662.

Fitzpatrick JM, Hill DL, Shyr Y, West J, Studholme C, Maurer CR Jr (1998): Visual assessment of the accuracy of retrospective registration of MR and CT images of the brain. IEEE Trans Med Imaging 17:571–585.

Hajnal JV, Saeed N, Soar EJ, Oatridge A, Young IR, Bydder GM (1995): A registration and interpolation procedure for subvoxel matching of serially acquired MR images. J Comput Assist Tomogr 19:289–296.

Hall WA, Truwit CL (2008): Intraoperative MR-guided neurosurgery. J Magn Reson Imaging 27:368–375.

Hastreiter P, Rezk-Salama C, Soza G, Bauer M, Greiner G, Fahlbusch R, Ganslandt O, Nimsky C (2004): Strategies for brain shift evaluation. Med Image Anal 8:447–464.

Irfanoglu MO, Modi P, Nayak A, Hutchinson EB, Sarlls J, Pierpaoli C (2015): DR-BUDDI (Diffeomorphic Registration for Blip-Up blip-Down Diffusion Imaging) method for correcting echo planar imaging distortions. Neuroimage 106:284–299.

Isgum I, Benders MJ, Avants B, Cardoso MJ, Counsell SJ, Gomez EF, Gui L, Huppi PS, Kersbergen KJ, Makropoulos A, Melbourne A, Moeskops P, Mol CP, Kuklisova-Murgasova M, Rueckert D, Schnabel JA, Srhoj-Egekher V, Wu J, Wang S, de Vries LS, Viergever MA (2015): Evaluation of automatic neonatal brain segmentation algorithms: The NeoBrainS12 challenge. Med Image Anal 20:135–151.

Jenkinson M, Smith S (2001): A global optimisation method for robust affine registration of brain images. Med Image Anal 5: 143–156.

Jezzard P, Balaban RS (1995): Correction for geometric distortion in echo planar images from B0 field variations. Magn Reson Med 34:65–73.

Klein S, Staring M, Murphy K, Viergever MA, Pluim JP (2010): elastix: A toolbox for intensity-based medical image registration. IEEE Trans Med Imaging 29:196–205.

Lipson AC, Gargollo PC, Black PM (2001): Intraoperative magnetic resonance imaging: Considerations for the operating room of the future. J Clin Neurosci 8:305–310.

Maesawa S, Fujii M, Nakahara N, Watanabe T, Wakabayashi T, Yoshida J (2010): Intraoperative tractography and motor evoked potential (MEP) monitoring in surgery for gliomas around the corticospinal tract. World Neurosurg 74: 153–161.

Maurer CR Jr, Hill DL, Martin AJ, Liu H, McCue M, Rueckert D, Lloret D, Hall WA, Maxwell RE, Hawkes DJ, Truwit CL (1998): Investigation of intraoperative brain deformation using a 1.5-T interventional MR system: Preliminary results. IEEE Trans Med Imaging 17:817–825.

Mendrik A, Vincken KL, Kuijf HJ, Breeuwer M, Bouvy WH, de Bresser J, Alansary A, de Bruijne M, Carass A, El-Baz A, Jog A, Katyal R, Khan AR, van der Lijn F, Mahmood Q, Mukherjee R, van Opbroek A, Paneri S, Pereira S, Persson M, Rajchl M, Sarikaya D, Smedby O, Silva CA, Vrooman HA, Vyas S, Wang C, Zhao L, Biessels GJ, Viergever MA (2015): MRBrainS Challenge: Online evaluation framework for brain image segmentation in 3T MRI scans. Comput Intell Neurosci 2015:1–16, doi:10.1155/2015/813696.

Murphy K, van Ginneken B, Reinhardt JM, Kabus S, Ding K, Deng X, Cao K, Du K, Christensen GE, Garcia V, Vercauteren T, Ayache N, Commowick O, Malandain G, Glocker B, Paragios N, Navab N, Gorbunova V, Sporring J, de Bruijne M, Han X, Heinrich MP, Schnabel JA, Jenkinson M, Lorenz C, Modat M, McClelland JR, Ourselin S, Muenzing SE, Viergever MA, De Nigris D, Collins DL, Arbel T, Peroni M, Li R, Sharp GC, Schmidt-Richberg A, Ehrhardt J, Werner R, Smeets D, Loeckx D, Song G, Tustison N, Avants B, Gee JC, Staring M, Klein S, Stoel BC, Urschler M, Werlberger M, Vandemeulebroucke J, Rit S, Sarrut D, Pluim JP (2011): Evaluation of registration methods on thoracic CT: The EMPIRE10 challenge. IEEE Trans Med Imaging 30:1901–1920.

Nabavi A, Black PM, Gering DT, Westin CF, Mehta V, Pergolizzi RS Jr, Ferrant M, Warfield SK, Hata N, Schwartz RB, Wells WM III, Kikinis R Jolesz FA (2001): Serial intraoperative magnetic resonance imaging of brain shift. Neurosurgery 48:787–797. discussion 797-8.

Nimsky C, Ganslandt O, Cerny S, Hastreiter P, Greiner G, Fahlbusch R (2000): Quantification of, visualization of, and compensation for brain shift using intraoperative magnetic resonance imaging. Neurosurgery 47:1070–1079. discussion 1079-80.

Nimsky C, Ganslandt O, Hastreiter P, Fahlbusch R (2001): Intraoperative compensation for brain shift. Surg Neurol 56:357–364. discussion 364-5.

Nimsky C, Ganslandt O, Hastreiter P, Wang R, Benner T, Sorensen AG, Fahlbusch R (2005): Intraoperative diffusion-tensor MR imaging: Shifting of white matter tracts during neurosurgical procedures–initial experience. Radiology 234:218–225.

Nimsky C, Ganslandt O, Hastreiter P, Wang R, Benner T, Sorensen AG, Fahlbusch R (2007): Preoperative and intraoperative diffusion tensor imaging-based fiber tracking in glioma surgery. Neurosurgery 61:178–185. discussion 186.

Nimsky C, Ganslandt O, Merhof D, Sorensen AG, Fahlbusch R (2006): Intraoperative visualization of the pyramidal tract by diffusion-tensor-imaging-based fiber tracking. Neuroimage 30: 1219–1229.

Otsu N (1975): A threshold selection method from gray-level histograms. Automatica 11:23–27.

Ozawa N, Muragaki Y, Nakamura R, Hori T, Iseki H (2009): Shift of the pyramidal tract during resection of the intraaxial brain tumors estimated by intraoperative diffusion-weighted imaging. Neurol Med Chir (Tokyo) 49:51–56.

Pfluger T, Vollmar C, Wismuller A, Dresel S, Berger F, Suntheim P, Leinsinger G, Hahn K (2000): Quantitative comparison of

automatic and interactive methods for MRI-SPECT image registration of the brain based on 3-dimensional calculation of error. J Nucl Med 41:1823–1829.

Romano A, D'Andrea G, Calabria LF, Coppola V, Espagnet CR, Pierallini A, Ferrante L, Fantozzi L, Bozzao A (2011): Pre- and intraoperative tractographic evaluation of corticospinal tract shift. Neurosurgery 69:696–704. discussion 704-5.

Sarkar A, Santiago RJ, Smith R, Kassaee A (2005): Comparison of manual vs. automated multimodality (CT-MRI) image registration for brain tumors. Med Dosim 30:20–24.

Smith SM, Jenkinson M, Woolrich MW, Beckmann CF, Behrens TE, Johansen-Berg H, Bannister PR, De Luca M, Drobnjak I, Flitney DE, Niazy RK, Saunders J, Vickers J, Zhang Y, De Stefano N, Brady JM, Matthews PM (2004): Advances in functional and structural MR image analysis and implementation as FSL. Neuroimage 23:S208–S219.

Smith SM, Zhang Y, Jenkinson M, Chen J, Matthews PM, Federico A, De Stefano N (2002): Accurate, robust, and automated longitudinal and cross-sectional brain change analysis. Neuroimage 17:479–489.

Strother SC, Anderson JR, Xu XL, Liow JS, Bonar DC, Rottenberg DA (1994): Quantitative comparisons of image registration techniques based on high-resolution MRI of the brain. J Comput Assist Tomogr 18:954–962.

Studholme C, Hill DL, Hawkes DJ (1996): Automated 3-D registration of MR and CT images of the head. Med Image Anal 1: 163–175.

Studholme C, Hill DL, Hawkes DJ (1997): Automated three-dimensional registration of magnetic resonance and positron emission tomography brain images by multiresolution optimization of voxel similarity measures. Med Phys 24:25–35.

Wells WM III, Viola P, Atsumi H, Nakajima S, Kikinis R (1996): Multi-modal volume registration by maximization of mutual information. Med Image Anal 1:35–51.

West J, Fitzpatrick JM, Wang MY, Dawant BM, Maurer CR Jr, Kessler RM, Maciunas RJ, Barillot C, Lemoine D, Collignon A, Maes F, Suetens P, Vandermeulen D, van den Elsen PA, Napel S, Sumanaweera TS, Harkness B, Hemler PF, Hill DL, Hawkes DJ, Studholme C, Maintz JB, Viergever MA, Malandain G, Pennec X, Noz ME, Maguire GQ Jr, Pollack M, Pelizzari CA, Robb RA, Hanson D, Woods RP, Woods RP (1997): Comparison and evaluation of retrospective intermodality brain image registration techniques. J Comput Assist Tomogr 21:554–566.

Woods RP, Cherry SR, Mazziotta JC (1992): Rapid automated algorithm for aligning and reslicing PET images. J Comput Assist Tomogr 16:620–633.

Woods RP, Grafton ST, Holmes CJ, Cherry SR, Mazziotta JC (1998): Automated image registration: I. General methods and intrasubject, intramodality validation. J Comput Assist Tomogr 22:139–152.

Woods RP, Mazziotta JC, Cherry SR (1993): MRI-PET registration with automated algorithm. J Comput Assist Tomogr 17:536–546.

Zack G, Rogers W, Latt S (1977): Automatic measurement of sister chromatid exchange frequency. J Histochem Cytochem 25:741–753.

Zuk TD, Atkins MS (1996): A comparison of manual and automatic methods for registering scans of the head. IEEE Trans Med Imaging 15:732–744.